TugSat: Removing Space Debris from Geostationary Orbits Using Solar Sails

Patrick W. Kelly,* Riccardo Bevilacqua,† and Leonel Mazal‡
University of Florida, Gainesville, Florida 32611-6250
and
Richard S. Erwin§
U.S. Air Force Research Laboratory, Albuquerque, New Mexico 87117-5776

DOI: 10.2514/1.A33872

Space debris accumulation is on the rise as commercial space applications become more affordable and existing satellites near the end of their operational lifetimes. For geosynchronous equatorial orbits, solar radiation pressure provides a unique solution for the removal of larger debris such as inoperable satellites. Given the current state of the art in solar sailing technology, a CubeSat can be tasked to deorbit satellites on the order of 1000 kg using a high-performance solar sail for propulsion. This CubeSat, called "TugSat," is simulated in this study, virtually deorbiting a satellite from geostationary orbit without the use of standard propulsion systems. This same TugSat can be reused indefinitely, between the geosynchronous equatorial orbit belt and the retirement orbit, to continuously remove debris from valuable geostationary orbit slots. The entire deorbit maneuver will demonstrate control of a satellite's semimajor axis, eccentricity, inclination, and geosynchronous equatorial orbit belt longitude: all using techniques to optimize time rates of change in the satellite's orbital elements. The TugSat concept provides a low-cost reusable means for geosynchronous equatorial orbit belt cleanup or open-ended geosynchronous equatorial orbit belt mission applications.

Nomenclature

A	=	surface area, km^2
a	=	semimajor axis, km
e	=	eccentricity
i	=	inclination, rad
J	=	cost function
m	=	mass, kg
$\hat{\boldsymbol{n}}$	=	sail surface normal unit vector
r	=	position magnitude, km
$\boldsymbol{r}$	=	position vector, km
U	=	candidate error function
u	=	argument of latitude, rad
v	=	velocity magnitude, km/s
$\boldsymbol{v}$	=	velocity vector, km/s
$\boldsymbol{x}$	=	state column vector (matrix notation)
$\boldsymbol{\zeta}$	=	orbital element parameter vector
θ	=	angle between sail surface normal and sun position vectors, rad
λ	=	longitude, rad
μ	=	gravitational parameter, km^3/s^2
ν	=	true anomaly, rad
$\boldsymbol{\sigma}$	=	state error
ϕ	=	phase angle, rad
ω	=	angular velocity rad/s
$\oplus$	=	Earth
$\mathbb{C}$	=	moon
$\odot$	=	sun

I. Introduction

ORBITAL debris accumulation is a topic of growing interest as the number of artificial satellites increases each year. Spent rocket bodies and dead satellites litter Earth orbits, threatening interference with operational satellites or increased fragmentation due to debris-to-debris collision. At geosynchronous equatorial orbits (GEOs), debris accumulation is not as severe as that present in low Earth orbits (LEOs); however, the GEO is operationally more restrictive due to its narrow dimensions. The Inter-Agency Space Debris Coordination Committee (IADC) has defined the dimensions of the GEO region as presented in Table 1 [1,2]. Satellites in this region do not experience atmospheric drag, so abandonment of assets in the GEO belt poses an indefinite problem for geostationary operations. It is common practice to deorbit end-of-life satellites to graveyard orbits above the GEO belt; however, orbital debris runs the risk of reentering the GEO belt due to the effects of solar radiation pressure (SRP). For these reasons, the IADC also establishes unique deorbit guidelines for satellites in the GEO belt, which are presented in Table 2 [1,2]. Unfortunately, only about one-third of end-of-life GEO satellites have been able to meet these recommendations because the vast majority of satellites experience subsystem failures over their lifetimes [3,4]. The Galaxy 15 incident is a highly publicized example of the orbital debris problem at GEO and the potential impact of space congestion on satellite operations [5]. As Galaxy 15 drifted through the GEO belt, multiple satellites were at risk of collision, requiring some to perform avoidance maneuvers. Although control was eventually regained for Galaxy 15, for many satellites, this is not possible.

To address unresponsive satellites, active debris removal methods have been developed to retrieve and deorbit unwanted bodies from orbit. For example, "Space Sweeper" is designed to eject LEO debris by harnessing the momentum exchange of plastic collisions to effectively sling orbital debris into lower orbit for eventual deorbit using atmospheric drag [6]. The Geosynchronous Large Debris Reorbiter GEO debris through the attraction of charged particles between a reorbiter spacecraft and the unwanted debris; by willfully maintaining an attractive force between the two bodies, GLiDeR can reorbit GEO debris to an acceptable graveyard orbit [7]. The focus of this paper also addresses maintenance of the GEO belt, harnessing SRP as the primary means of propulsion to perform repeated deorbit of orbital debris. The proposed satellite concept, called TugSat, will use a large, highly reflective solar sail to maneuver

Table 1   Protected GEO belt region

Property	Value
GEO altitude	35,786 km
Lower altitude	GEO − 200 km
Upper altitude	GEO + 200 km
Inclination	±15 deg

Table 2   GEO region disposal guidelines

Property	Requirements
Perigee altitude	$\leq$GEO + 235 km + $(1000 \cdot C_R \cdot (A/m))$
	235 km: sum of the upper altitude of the GEO protected region (200 km) and the maximum descent of a reorbited spacecraft due to lunisolar and geopotential perturbations (35 km)
	C_R: solar radiation pressure coefficient, 1 ∼ 1.5
	A/m: aspect area to dry mass (m^2/kg)
Eccentricity	$\leq$0.003

a deorbiter satellite, with captured payload, to a disposal orbit beyond the GEO belt. TugSat can then be reorbited to GEO for rendezvous in a desired GEO slot for capture of another drifting payload.

Using environmental forces to enhance satellite operation has been the topic of many works, leading to interesting methods of satellite control ranging from semimajor axis control using the Earth's magnetic field [8] to satellite formation control by means of atmospheric drag [9]. Control of spacecraft in this manner can reduce propellant dependencies, minimize control efforts, or extend satellite life spans. This paper is concerned with the viability of orbital control of a satellite using the momentum exchange of sunlight. With the absence of atmospheric drag, the next most significant nonconservative perturbation is SRP. The results presented here will prove orbital debris removal can be performed using solar sails, providing free and near-infinite delta-V and allowing for repeated characterization of a satellite's orbit by means of semimajor axis, eccentricity, inclination, and longitude control.

Solar radiation pressure has already been proven a capable means of propulsion, especially in the formation of exotic non-Keplerian orbits or interplanetary transfer orbits [10,11]. Many works focus on sail applications in a heliocentric sense, determining optimal guidance, solutions to orbit transfers within the solar system, or even thrust vector control strategies using sail orientation [12–14]. Unfortunately, heliocentric solutions do not directly translate to planetocentric environments; therefore, it is necessary to derive separate techniques for more practical applications. Earth-orbiting solar sailing applications have been proposed for assistance in satellite disposal for low Earth orbits [15] or medium Earth orbits [16], as well as escape from geosynchronous orbits [17]. These maneuvers are achieved by aligning a solar sail to alter a satellite's orbital velocity to raise or lower the satellite's altitude. Specific strategies for changes in semimajor axis and eccentricity were given in [18], illustrating appropriate satellite orientations throughout the orbit, based on the relative position between the spacecraft and the sun. It is clear from these findings that acceleration and velocity vector geometries play a key role in controlling the effect of applied SRP forces. In an effort to address the orbital debris problem, this research presents a geometrical method for optimizing the rates of change in the orbital elements that are necessary to successfully deorbit a defunct satellite. To address the challenge of satellite placement into orbital slots in the GEO belt, the control techniques will also be used to perform targeting of GEO belt longitudes. Unlike heliocentric applications, the methods presented here do not benefit from fixed sun locations; therefore, solutions are inherently nonlinear and do not lend themselves to the same analytical elegance presented in the plethora of heliocentric works.

The current state of the art in solar sailing technology is demonstrated with such examples as the Japan Aerospace Exploration Agency's (JAXA's) Interplanetary Kite-craft Accelerated by Radiation Of the Sun (IKAROS) [19], the Planetary Society's LightSail-1 [20], and NASA's Sunjammer [21]. JAXA's IKAROS in particular is the first

satellite to use solar radiation pressure as its primary means of propulsion and is capable of attitude and orbit control using a high-performance solar sail. LightSail-1 was a $10 \times 10 \times 34$ cm, or 3U, CubeSat that successfully deployed a highly reflective, 32 m^2 solar sail in LEO before tumbling back into Earth's atmosphere after seven days of orbit. Sunjammer boasts the largest solar sail ever constructed, weighing 32 kg with a 38×38 m solar sail and a surface area of over 1200 m^2. With these satellites in mind, other ambitious uses for solar sailing satellites are presented in the body of this study.

The TugSat concept introduces a sail-propelled deorbit method using a nonlinear controller. This controller produces sail orientations capable of tracking desired semimajor axis, eccentricity, inclination, and longitude values as necessary to achieve satellite deorbit and GEO slot rendezvous. This is achieved by optimizing time derivatives for the satellite's orbital elements based on the satellite's SRP exposure using the Gaussian variation of parameters (VOPs) equations. Key geometric relationships between the satellite's acceleration and orbital velocity vectors will dictate the implementation of these optimized sail orientations. These orientations are validated using Monte Carlo simulations. Ultimately, through a combination of sail-based maneuvers, the TugSat simulation will demonstrate deorbit of defunct satellites from the GEO belt, as well as placement of the deorbiter satellite into desired slots within the GEO belt. Throughout these maneuvers, thrusters are only assumed necessary to dump momentum during attitude control of the solar sail [22]. The entire mission is considered successful once the deorbiter reenters the GEO belt, as defined by the IADC, at the correct longitude. From here, an appropriate relative motion model using Clohessy–Wiltshire equations or relative orbital elements can be employed to address the challenge of satellite docking and rendezvous with another defunct satellite. The satellite rendezvous problem is not addressed in this body of work.

The remainder of the paper is organized as follows: Sec. II introduces the dynamics of a satellite operating at geosynchronous altitudes, Sec. III addresses the control techniques employed to manipulate key orbital elements, Sec. IV outlines the TugSat mission concept, and Sec. V provides a summary of the findings presented in the previous sections.

II.   Satellite Dynamics Model

A.   Force Model

The dynamics model for the GEO orbit includes three gravitational contributions and one nongravitational perturbation. Gravitational influences come from the Earth's gravity, which includes the $C_{2,0}$ and $C_{2,2}$ gravitational harmonic coefficients, and third-body perturbations from the moon and sun. Acceleration from the solar radiation pressure is the only nongravitational perturbation and acts as the control input for the maneuvers presented in Secs. III and IV.

The total acceleration acting on the satellite can then be described as

$$\ddot{\boldsymbol{r}} = \ddot{\boldsymbol{r}}_{\oplus} + \ddot{\boldsymbol{r}}_{\mathbb{C}} + \ddot{\boldsymbol{r}}_{\odot} + \ddot{\boldsymbol{r}}_{\mathrm{SRP}} \tag{1}$$

As illustrated by Montenbruck and Gill ([23] p. 55), the Earth's gravitational acceleration at GEO is on the order of 10^{-2} km/s^2, with oblateness contributions on the order of 10^{-6} km/s^2 and 10^{-10} km/s^2 for $C_{2,0}$ and $C_{2,2}$, respectively. The effects of the sun and moon exhibit accelerations on the order of 10^{-8} km/s^2. Geostationary satellites, with typical area-to-mass ratios on the order of 0.01 m^2/kg, experience SRP perturbations on the order of 10^{-10} km/s^2. This magnitude poorly competes with the gravitational accelerations; however, by increasing the area-to-mass ratio of the satellite, the magnitude of the experienced SRP acceleration can increase to match or even overcome the effects of the sun and moon.

The Earth-based accelerations expressed in an Earth-centered Earth-fixed (ECEF) principal axis coordinate system are

$$\ddot{\boldsymbol{r}}_{\oplus} = 2\omega_{\oplus} \begin{bmatrix} \dot{y} \\ -\dot{x} \\ 0 \end{bmatrix} + \omega_{\oplus}^2 \begin{bmatrix} x \\ y \\ 0 \end{bmatrix} - \nabla\Psi \tag{2}$$

with

$$\Psi = -\frac{\mu}{r}\left[1 + \left(\frac{\bar{\alpha}}{r}\right)^2\left\{3C_{2,2}\frac{x^2 - y^2}{r^2} - \frac{1}{2}C_{2,0}\left(1 - 3\frac{z^2}{r^2}\right)\right\}\right] \quad (3)$$

where $\omega_\oplus$ is the angular velocity of the Earth; x, y, and z are the satellite's position coordinates in the principal axis coordinate system; and Ψ is the gravitational potential from the Earth, with the gravitational parameter μ, mean radius of the Earth $\bar{\alpha}$, gravitational harmonic coefficients $C_{2,0}$ and $C_{2,2}$, and satellite position magnitude r. The principal axis coordinate system is the standard ECEF coordinate system rotated -14.93 deg about its $\hat{z}$ axis [24]. The behavior of a satellite under the influence of these Earth dynamics was examined by Lara and Elipe [25]. From Vallado ([26] p. 575), third-body perturbations can be modeled as

$$\ddot{\boldsymbol{r}}_k = -\frac{\mu_k}{r_{\oplus k}^3}\left[\boldsymbol{r} - \left\{3\frac{\boldsymbol{r}\cdot\boldsymbol{r}_{\oplus k}}{r_{\oplus k}^2} - \frac{15}{2}\left(\frac{\boldsymbol{r}\cdot\boldsymbol{r}_{\oplus k}}{r_{\oplus k}^2}\right)^2\right\}\boldsymbol{r}_{\oplus k}\right] \quad (4)$$

where μ_k is the gravitational parameter for third-body k, and $\boldsymbol{r}_{\oplus k}$ is the position vector of third-body k (with magnitude $r_{\oplus k}$) as measured from an Earth-centered inertial (ECI) coordinate system. The ECI expression for acceleration due to SRP is modeled by Montenbruck and Gill ([23] p. 81) as

$$\ddot{\boldsymbol{r}}_{\text{SRP}} = -\kappa P_\odot\frac{\text{AU}^2}{r_\odot^2}\frac{A}{m}\cos\theta[(1-\varepsilon)\hat{\boldsymbol{r}}_\odot + 2\varepsilon\cos\theta\hat{\boldsymbol{n}}], \quad \theta \in \left[0, \frac{\pi}{2}\right] \quad (5)$$

with the solar radiation pressure magnitude $P_\odot$, the satellite distance from the sun r, the astronomical unit (AU), the shadow coefficient κ (from the moon and the Earth), the reflectivity coefficient ε, the area-to-mass ratio A/m, and the angle θ between the sun direction vector $\hat{\boldsymbol{r}}_\odot$ (as measured from the satellite) and the sail surface normal $\hat{\boldsymbol{n}}$. Because the sail normal direction is measured from the surface facing the sun, θ is restricted to values between zero and $\pi/2$. For Earth orbits, the solar radiation pressure $P_\odot$ is approximately 4.57×10^{-6} N/m^2 and can be scaled based on the instantaneous distance between the satellite and the sun $(\text{AU}^2/r_\odot^2)$. Under a few assumptions, $\text{AU}^2/r_\odot^2 \approx 1, \kappa = 1, \varepsilon = 1$, a characteristic acceleration can be defined as

$$a_c = 2P_\odot\frac{A}{m} \quad (6)$$

and Eq. (5) takes the approximate form

$$\ddot{\boldsymbol{r}}_{\text{SRP}} \approx -a_c\cos^2\theta\hat{\boldsymbol{n}}, \quad \theta \in \left[0, \frac{\pi}{2}\right] \quad (7)$$

From Eq. (7), it is clear that the magnitude of the experienced SRP acceleration directly depends on the orientation of the sail surface normal. The direction of the SRP acceleration can be determined as a result of assuming perfect reflectivity ($\varepsilon = 1$). Due to the specular reflection of incident photons, the satellite will experience an SRP force acting in the direction opposite that of the sail surface normal, thrusting in the $-\hat{\boldsymbol{n}}$ direction. In this way, the SRP force can be directed in any direction negatively aligned with the sun position vector. Sail alignment at $\theta = 0$ (surface normal in line with the sun position vector) will produce maximum SRP magnitudes, directed away from the sun. Orientations with $\theta = (\pi/2)$ (sail perpendicular to the sun) experience minimal accelerations, making it possible to "turn off" SRP, assuming negligible accelerations acting on the satellite bus structure. Intermediate orientations will result in SRP accelerations acting in the direction opposite the sail surface normal with decreasing magnitudes as θ approaches $\pi/2$. Figure 1 illustrates the relationship between the experienced SRP force and the sun direction vector.

In the upcoming sections, simulations are based off a 50 kg satellite equipped with a perfectly reflective, 800 m^2 (approximately 28×28 m) solar sail. This area is based on attainable sail sizes and desirable area-to-mass ratios, given the current state of the art for solar
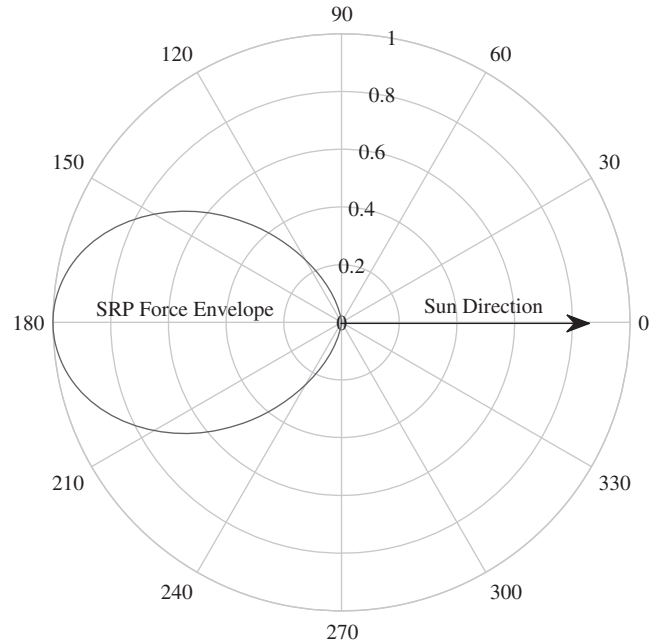
Fig. 1 Two-dimensional polar representation of the SRP force envelope based on sun direction. Radial magnitudes are fractions of the maximum available SRP force.

sailing satellites. With the additional mass of a 1000 kg payload, the area-to-mass ratio of the total system is 0.76 m^2/kg, resulting in a characteristic acceleration of approximately 6.95×10^{-9} km/s^2 at GEO.

B. Gaussian Variation of Parameters

The satellite control logic will make use of time derivatives for the satellite's orbital elements to characterize the response of the semimajor axis, eccentricity, and inclination to solar radiation pressure. Expressions for these rates of change can be determined using the Gaussian variation of parameters formulas as detailed in ([26] p. 636). The VOP equations of interest are expressed in the following manner:

$$\frac{da}{dt} = \frac{2}{n\sqrt{1-e^2}}\left\{e\sin(\nu)F_R + \frac{p}{r}F_S\right\}$$

$$\frac{de}{dt} = \frac{\sqrt{1-e^2}}{na}\left\{\sin(\nu)F_R + \left(\cos(\nu) + \frac{e+\cos(\nu)}{1+e\cos(\nu)}\right)F_S\right\}$$

$$\frac{di}{dt} = \frac{r\cos(u)}{na^2\sqrt{1-e^2}}F_W \quad (8)$$

where n is the mean motion, p is the semiparameter, and u is the argument of latitude. The perturbing forces, F_R, F_S, and F_W are components of the specific force vector $\boldsymbol{F}$ in the local vertical, local horizontal coordinate system with $\hat{\boldsymbol{R}}$ pointing along the position vector of the satellite, $\hat{\boldsymbol{S}}$ in the orbit plane perpendicular to $\hat{\boldsymbol{R}}$ and in the direction of satellite motion, and $\hat{\boldsymbol{W}} = \hat{\boldsymbol{R}} \times \hat{\boldsymbol{S}}$. Equation (8) can be written in matrix form as the product of two matrices $\mathbf{Z}$ and $\mathbf{F}$ defined as

$$\mathbf{Z} = \begin{bmatrix} \frac{2}{n\sqrt{1-e^2}}e\sin(\nu) & \frac{2}{n\sqrt{1-e^2}}\frac{p}{r} & 0 \\ \frac{\sqrt{1-e^2}}{na}\sin(\nu) & \frac{\sqrt{1-e^2}}{na}\left(\cos(\nu) + \frac{e+\cos(\nu)}{1+e\cos(\nu)}\right) & 0 \\ 0 & 0 & \frac{r\cos(u)}{na^2\sqrt{1-e^2}} \end{bmatrix}$$

$$(9)$$

and

$$\mathbf{F} = [\, F_R \quad F_S \quad F_W \,]^T \tag{10}$$

resulting in

$$\dot{\mathbf{q}} = \mathbf{ZF} \tag{11}$$

where

$$\mathbf{q} = [\, a \quad e \quad i \,]^T \tag{12}$$

The rows of the $\mathbf{Z}$ matrix can be thought of as row vectors $\boldsymbol{\zeta}_q$ corresponding to a specific orbital element $q \in \{a, e, i\}$:

$$\boldsymbol{\zeta}_q = [\, \zeta_{q,R} \quad \zeta_{q,S} \quad \zeta_{q,W} \,] \tag{13}$$

$$\mathbf{Z} = [\, \boldsymbol{\zeta}_a^T \quad \boldsymbol{\zeta}_e^T \quad \boldsymbol{\zeta}_i^T \,]^T \tag{14}$$

These expressions will be used to determine sail orientations that help achieve desired semimajor axis, eccentricity, and inclination values for a solar sailing satellite. Note the state dependence of $\mathbf{Z}$.

III. Optimized Sail Orientation

As described in the previous section, the exerted SRP force can only oppose the sun position vector ($\ddot{\boldsymbol{r}}_{\mathrm{SRP}} \cdot \hat{\boldsymbol{r}}_\odot < 0$). This adds a significant performance constraint by removing any solutions requiring a control input with a positive SRP force component along the sun position vector. To add further complications, the force magnitude is not uniform across all sail angles: $\theta \in [0, (\pi/2)]$. These constraints result in underactuated low-thrust satellite maneuvering. Given these complex, nonlinear equations and stringent constraints, the formulation and solution as a direct optimal control problem are considered infeasible. Additionally, a formal Lyapunov-based control scheme is unattainable due to the irregular availability of SRP and the inability to continuously overcome gravitational disturbances from the Earth, moon, and sun. As a result, the developed method will address control of a satellite's orbital elements sequentially, accepting any coupled effects on the remaining orbital elements as well as disturbances from the third bodies and Earth's oblateness. Controlling the satellite's orbit in this manner requires careful consideration of the order in which to address each orbital element, and it does not result in precise tracking of a desired state. For the TugSat mission in particular, it is only necessary to deorbit, reorbit, and target specific GEO belt slots using SRP. These tasks have broad requirements for a, e, i, and longitude values; and they have no restriction on Ω, ω, and ν values.

A new coordinate system will now be introduced to optimize $\dot{q}$ based on the sun direction unit vector $\hat{\boldsymbol{r}}_\odot$ and a VOP vector $\boldsymbol{\zeta}$ made up of the components of $\boldsymbol{\zeta}_q^T$. New basis vectors are defined as follows:

$$\hat{\boldsymbol{e}}_1 = \hat{\boldsymbol{r}}_\odot \tag{15}$$

$$\hat{\boldsymbol{e}}_2 = \frac{\boldsymbol{\zeta} - (\boldsymbol{\zeta} \cdot \hat{\boldsymbol{r}}_\odot)\hat{\boldsymbol{r}}_\odot}{\|\boldsymbol{\zeta} - (\boldsymbol{\zeta} \cdot \hat{\boldsymbol{r}}_\odot)\hat{\boldsymbol{r}}_\odot\|} \tag{16}$$

$$\hat{\boldsymbol{e}}_3 = \hat{\boldsymbol{e}}_1 \times \hat{\boldsymbol{e}}_2 \tag{17}$$

In this coordinate system, an angle α is formed between $\hat{\boldsymbol{e}}_1$ and the projection of $\hat{\boldsymbol{n}}$ in the $\hat{\boldsymbol{e}}_1$–$\hat{\boldsymbol{e}}_2$ plane, an angle β is formed between $\hat{\boldsymbol{e}}_1$ and $\boldsymbol{\zeta}$, and an angle δ is formed between the $\hat{\boldsymbol{e}}_1$–$\hat{\boldsymbol{e}}_2$ plane and $\hat{\boldsymbol{n}}$. These relationships are illustrated in Fig. 2. With this new basis, the following vector relationships can be determined:

$$\hat{\boldsymbol{n}} = \cos \alpha \cos \delta \hat{\boldsymbol{e}}_1 + \sin \alpha \cos \delta \hat{\boldsymbol{e}}_2 + \sin \delta \hat{\boldsymbol{e}}_3 \tag{18}$$

$$\hat{\boldsymbol{r}}_\odot \cdot \hat{\boldsymbol{n}} = \cos \alpha \cos \delta \tag{19}$$
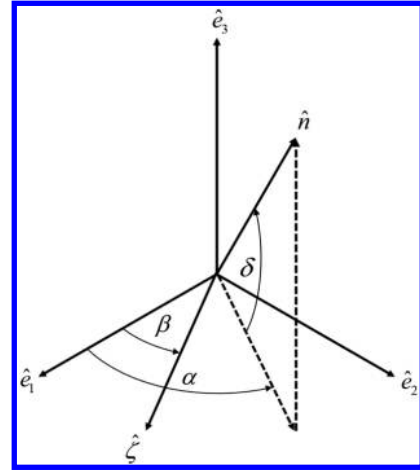

Fig. 2   Illustration of vector relationships for optimized sail orientation.

$$\boldsymbol{\zeta} \cdot \hat{\boldsymbol{n}} = \|\boldsymbol{\zeta}\|[\cos \beta \cos \alpha \cos \delta + \sin \beta \sin \alpha \cos \delta] \tag{20}$$

where $\|\boldsymbol{\zeta}\|$ is the magnitude of the parameter vector $\boldsymbol{\zeta}$.

Recall, from Eq. (11), that the change in an orbital element q due to SRP is

$$\dot{q} = \boldsymbol{\zeta}_q \mathbf{F}_{\mathrm{SRP}} \tag{21}$$

Using Eq. (7) to model the specific force due to SRP results in

$$\dot{q} = -(a_c \cos^2 \theta) \boldsymbol{\zeta}_q \hat{\mathbf{n}} \tag{22}$$

where $\hat{\mathbf{n}}$ is the matrix equivalent to $\hat{\boldsymbol{n}}$. From Eqs. (18–20), Eq. (22) can be expressed in terms of angles α, β, and δ:

$$\dot{q} = -a_c \|\boldsymbol{\zeta}\| \cos^3 \delta[\cos^2 \alpha(\cos \alpha \cos \beta + \sin \alpha \sin \beta)]$$
$$= -\rho \cos^3 \delta[\cos^2(\alpha) \cos(\alpha - \beta)] \tag{23}$$

where ρ is the product of the characteristic acceleration a_c and the VOP vector magnitude $\boldsymbol{\zeta}$. To calculate the extrema of Eq. (23), it is required that $\cos \delta = 1 \rightarrow \delta = 0$, restricting $\hat{\boldsymbol{n}}$ to the $\hat{\boldsymbol{e}}_1$–$\hat{\boldsymbol{e}}_2$ plane and resulting in

$$\hat{\boldsymbol{n}} = \cos \alpha \hat{\boldsymbol{e}}_1 + \sin \alpha \hat{\boldsymbol{e}}_2 \tag{24}$$

Because $\hat{\boldsymbol{r}}_\odot \cdot \hat{\boldsymbol{n}} \geq 0$, it follows that $\alpha \in [-\pi/2, \pi/2]$. A cost function J can now be defined as

$$J = \cos^2(\alpha) \cos(\alpha - \beta) \tag{25}$$

which can be used to optimize Eq. (23) and yield instantaneous maximum rates of change in q. With β determined by the sun position vector $\hat{\boldsymbol{e}}_1$ and the parameter vector $\boldsymbol{\zeta}$, α is the only controllable angle in J. As a result, the solution space for potential control inputs varies as the satellite orbits the Earth. The desired α angle can be determined over the range $[-\pi/2, \pi/2]$, which either minimizes or maximizes J. Equation (24) will give the desired sail orientation using the optimized α angle. Using Eq. (25), instantaneous maximum or minimum rates of change can be attained for the satellite's orbital elements.

To achieve a desired orbital element value q_d, Eq. (25) can be augmented. First, define the element error σ_q as the difference between the actual and desired orbital element values:

$$\sigma_q = q - q_d \tag{26}$$

To reduce this error, a nonnegative scalar function U is developed as

$$U = \frac{1}{2} \sigma_q^2 \tag{27}$$

with derivative

$$\dot{U} = \sigma_q \dot{\sigma}_q \qquad (28)$$

The control input can be determined through $\dot{\sigma}_q$ and should be designed to make $\dot{U}$ negative. This can be achieved by setting $\dot{\sigma}_q$ equal to a scaled negative of σ_q

$$\dot{\sigma}_q = -k\sigma_q \qquad (29)$$

with scaling constant $k > 0$, resulting in

$$\dot{U} = -k\sigma_q^2 \qquad (30)$$

which is a nonpositive derivative. In the development that follows, the sail orientation angle θ will be determined such that Eq. (29) is achieved, thereby proving convergence of the error σ_q toward zero.

Recall, from Eq. (8), that the orbital element error time derivative can be expressed in the following form:

$$\dot{\sigma}_q = \zeta_{q,R} F_R + \zeta_{q,S} F_S + \zeta_{q,W} F_W = \boldsymbol{\zeta}_q \mathbf{F} \qquad (31)$$

The specific force $\mathbf{F}$ contains contributions from the gravitational harmonic coefficients, third bodies, and solar radiation pressure. Grouping the gravitational contributions together in $\mathbf{F}_{\text{grav}}$, the specific force can be rewritten as

$$\mathbf{F} = \mathbf{F}_{\text{grav}} + \mathbf{F}_{\text{SRP}} \qquad (32)$$

resulting in

$$\dot{\sigma}_q = \boldsymbol{\zeta}_q (\mathbf{F}_{\text{grav}} + \mathbf{F}_{\text{SRP}})$$
$$= \boldsymbol{\zeta}_q \mathbf{F}_{\text{grav}} + \boldsymbol{\zeta}_q \mathbf{F}_{\text{SRP}} \qquad (33)$$

Introducing D as the product of $\boldsymbol{\zeta}_q$ and F_{grav}, and once again using Eqs. (22) and (23), the error derivative becomes

$$\dot{\sigma}_q = D - (a_c \cos^2\theta) \boldsymbol{\zeta}_q \hat{\mathbf{n}} \qquad (34)$$

From Eqs. (23) and (29), the error derivative can be expressed in terms of σ_q and angles α, β, and δ:

$$-k\sigma_q = D - \rho \cos^3(\delta) \cos^2(\alpha) \cos(\alpha - \beta) \qquad (35)$$

Isolating the α terms, Eq. (35) produces

$$\frac{D + k\sigma_q}{\rho} = \cos^3(\delta) \cos^2(\alpha) \cos(\alpha - \beta) \qquad (36)$$

with $\cos^3(\delta) \cos^2(\alpha) \cos(\alpha - \beta)$ bounded between $[-1, 1]$. Recalling that D, ρ, and β are dictated by geometry, values for k, δ, and α must be determined to achieve Eq. (36). Notice that, regardless of the design of the scaling constant k, no guarantees can be made to bound the left side of Eq. (36) between $[-1, 1]$ due to the uncertainty (in both sign and relative magnitude) of the disturbance D. Orientations that isolate beneficial components of the available solar radiation force vector often do not produce strong enough SRP accelerations to continuously overcome the gravitational disturbances. Ultimately, without the use of unrealistic, very large solar sails, the experienced solar radiation pressure is not guaranteed to be the dominant perturbation. For this reason, Monte Carlo simulations are employed to prove the effectiveness of this control strategy. The determination of an analytic stability proof for this controller is ongoing, and is a separate research topic beyond the scope of this paper. To best achieve Eq. (36), $\hat{\boldsymbol{n}}$ will once again be restricted to the $\hat{\boldsymbol{e}}_1$–$\hat{\boldsymbol{e}}_2$ plane by choosing $\delta = 0$. The scaling constant k is a flexible design choice, chosen to weight control of the error against the effects of D. The augmented cost function becomes

$$J_q = \left| \frac{D + k\sigma_q}{\rho} - \cos^2(\alpha) \cos(\alpha - \beta) \right| \qquad (37)$$

to be minimized numerically across the interval

$$\alpha \in \left[-\frac{\pi}{2}, \frac{\pi}{2} \right]$$

because no analytical solution exists for Eq. (37).

Toggling control between the orbital elements in this manner results in switched system-like behavior. The state evolution can be interpreted to switch between two sets of dynamics: a system under the influence of SRP, and a system free of SRP. A nested layer of switching exists within the SRP dynamics, where the sail orientations work to enhance changes in a specific orbital element. In a general sense, the orientations utilize only the desirable effects of the solar radiation pressure. When no desirable SRP contributions exist within a given SRP solution space (e.g., all possible sail orientations result in an increase in semimajor axis when attempting to decrease the satellite's semimajor axis), the solar sail is oriented perpendicular to the incoming sunlight, minimizing the contribution from the SRP force.

IV. TugSat

The TugSat simulation will demonstrate the potential to remove orbital debris from the GEO belt using a solar sailing satellite. Recall that TugSat is simulated as a 50 kg satellite equipped with an 800 m² solar sail, resulting in an area-to-mass ratio of 16 m²/kg. In simulation, the satellite will be deorbiting a 1000 kg payload, decreasing the area-to-mass ratio of the total system to 0.76 m²/kg. Initialized in equatorial orbit within the GEO belt, TugSat will begin by raising the semimajor axis of its orbit by 350 km. Once the semimajor axis target is achieved, TugSat will begin reducing the eccentricity of its new orbit while maintaining an altitude above the IADC guidelines for graveyard orbits. Next, TugSat will release the 1000 kg payload and begin descent back to the GEO belt, targeting a desired GEO belt longitude for rendezvous with another payload. These maneuvers will be executed using the optimized sail orientations and implemented under the full dynamics model as described in Sec. II. The following simulations will expand upon the TugSat maneuvers while demonstrating switched control of the semimajor axis, eccentricity, inclination, and longitude.

A. Semimajor Axis

The first goal for deorbit using TugSat is to increase the semimajor axis of the payload. An increase in the semimajor axis will result in an increase in the satellite's apogee and a net increase in the satellite's average orbital altitude. For tracking of a desired semimajor axis a_d, the error function is written as

$$U = \frac{1}{2}\sigma_a^2$$
$$= \frac{1}{2}(a - a_d)^2 \qquad (38)$$

with

$$\dot{U} = \sigma_a \dot{\sigma}_a$$
$$= (a - a_d)\dot{a} \qquad (39)$$

The expression for $\dot{a}$ is known from Eq. (8), and the semimajor axis error can be found using the methods described in Sec. III. Implementing the semimajor axis orientations results in the behaviors illustrated in Fig. 3.

To verify the reliability of these orientations, 1000 simulations were performed to target a desired semimajor axis. These simulations were configured using uniformly randomized initial conditions as detailed in Table 3. These initial conditions place the satellite within 200 km of the GEO altitude and 1° latitude of the GEO slot. All simulations result in successful error convergence as illustrated in Fig. 4.
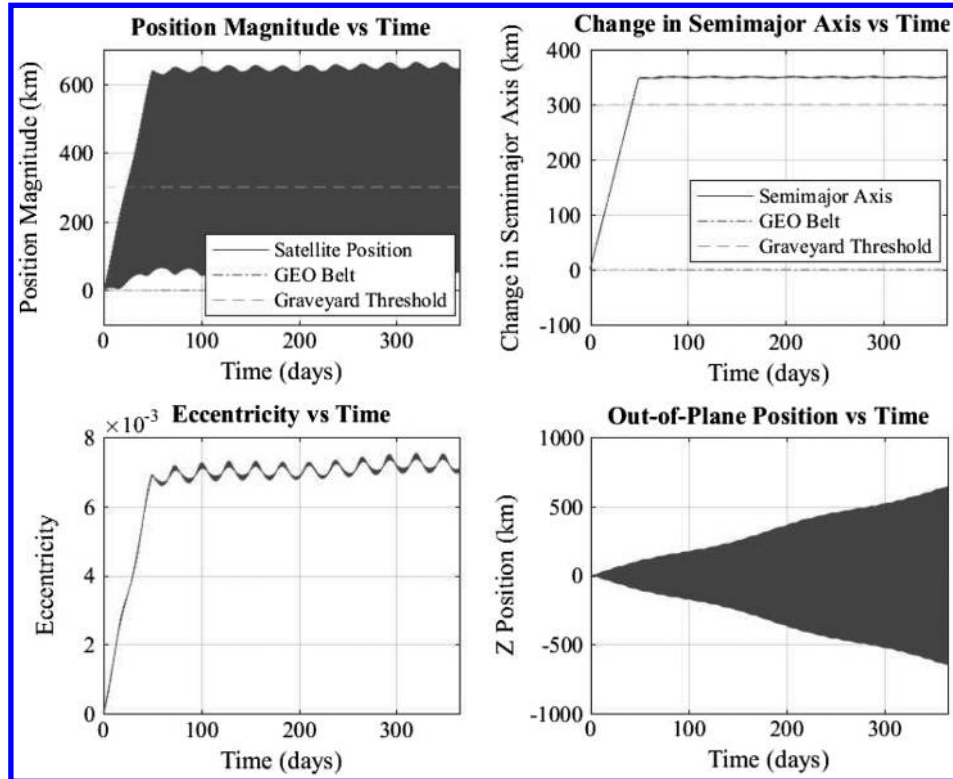
Fig. 3   Sail orientations to increase the semimajor axis. Position and semimajor axis values are zeroed at the GEO belt.

B. Eccentricity

Once the desired semimajor axis is attained, the eccentricity must be reduced so that both perigee and apogee values remain above the graveyard orbit threshold. Two methods are now presented.

1. Greedy Approach

The error function corresponding to eccentricity control is

$$U = \frac{1}{2}\sigma_e^2$$
$$= \frac{1}{2}(e - e_d)^2 \tag{40}$$

with

$$\dot{U} = \sigma_e\dot{\sigma}_e$$
$$= (e - e_d)\dot{e} \tag{41}$$

where e_d is the desired eccentricity. The expression for $\dot{e}$ is known from Eq. (8), and the sail orientations to minimize the eccentricity error can be found using the methods described in Sec. III. Implementing these orientations can reduce the eccentricity as illustrated in Fig. 5.
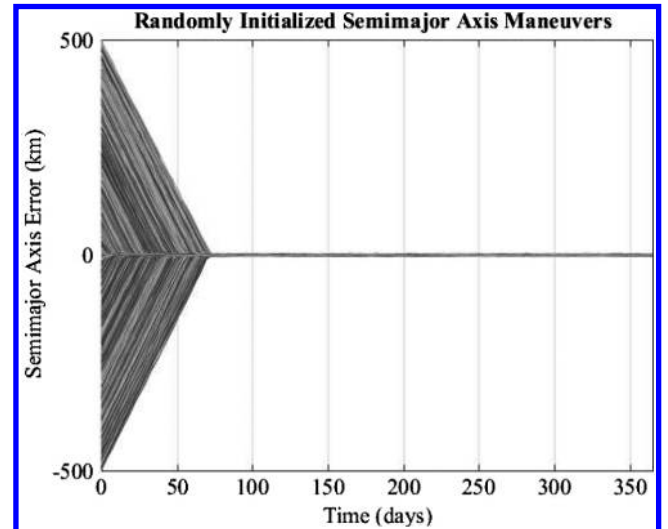

Fig. 4   Performance results of 1000 simulations to target desired semimajor axis.

To validate these orientations, 1000 simulations were executed with initial conditions described in Table 4. As displayed in Fig. 6, eccentricity values can be reduced to steady-state values of around $e = 1.75 \times 10^{-3}$, corresponding to a difference of 160 km between apogee and perigee values, using these orientations.

2. Velocity Monitoring

For smaller A/m, eccentricity reduction using SRP can be improved through a partnering with the existing gravitational accelerations. Recall that the satellite dynamics are dominated by these gravitational effects. These accelerations persist and cannot be controlled; however, their effects on the satellite orbit can be enhanced using SRP. In simulations, it was noted that, if the eccentricity control was modified as follows, a lower transient response resulted.
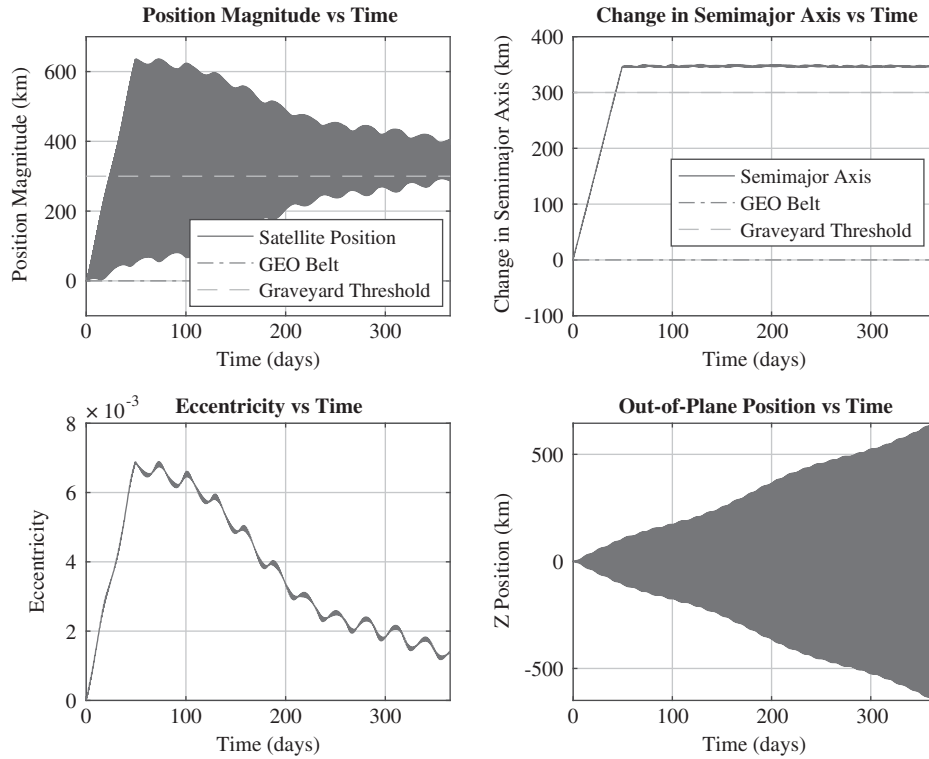
Table 3   Simulation properties for semimajor axis control tests[a]

Orbital elements		Range
a_0	Semimajor axis	42,164 km
e_0	Eccentricity	$\in [0, 0.005]$
i_0	Inclination	$\in [-0.0175, 0.0175]$ rad
Ω_0	Right ascension of the ascending node	$\in [0, 2\pi]$ rad
ω_0	Argument of perigee	$\in [0, 2\pi]$ rad
ν_0	True anomaly	$\in [0, 2\pi]$ rad
a_d	——	$a_0 \pm 500$ km

[a]Simulation durations of one year, initialized between the years 2000 and 2020.

Fig. 5   Sail orientations to minimize eccentricity after raising semimajor axis. Position and semimajor axis values are zeroed at the GEO belt.

To begin, note the characteristic velocity of a circular orbit (neglecting perturbations) in terms of semimajor axis and gravitational parameter:

$$v_{\text{circular}} = \sqrt{\frac{\mu}{a}} \qquad (42)$$

By polling the orbital velocity, it can be determined whether to accelerate or decelerate the satellite by comparing the velocity to the value given by Eq. (42). Solar radiation pressure can be used to amplify the desirable effects from the gravitational accelerations, accelerating or decelerating the satellite as necessary. A velocity-monitoring algorithm is now presented to determine when to implement the eccentricity orientations for improved reduction of eccentricity:

if

$$\boldsymbol{v} \cdot \boldsymbol{a}_{\text{gravity}} > 0 \quad \text{and} \quad \boldsymbol{v} \cdot \hat{\boldsymbol{r}}_{\odot} < 0 \quad \text{and} \quad v < v_{\text{circular}}$$

or

$$\boldsymbol{v} \cdot \boldsymbol{a}_{\text{gravity}} < 0 \quad \text{and} \quad \boldsymbol{v} \cdot \hat{\boldsymbol{r}}_{\odot} > 0 \quad \text{and} \quad v > v_{\text{circular}}$$

then

$$\hat{\boldsymbol{n}} = \cos \alpha \hat{\boldsymbol{e}}_1 + \sin \alpha \hat{\boldsymbol{e}}_2 \qquad (43)$$

Table 4   Simulation properties for eccentricity reduction tests[a]

Parameter	Range
a_0	$42{,}164 \pm 500$ km
e_0	$\in [0, 0.015]$
i_0	$\in [-0.0175, 0.0175]$ rad
Ω_0	$\in [0, 2\pi]$ rad
ω_0	$\in [0, 2\pi]$ rad
ν_0	$\in [0, 2\pi]$ rad
e_d	0

[a]Simulation durations of two years, initialized between the years 2000 and 2020.
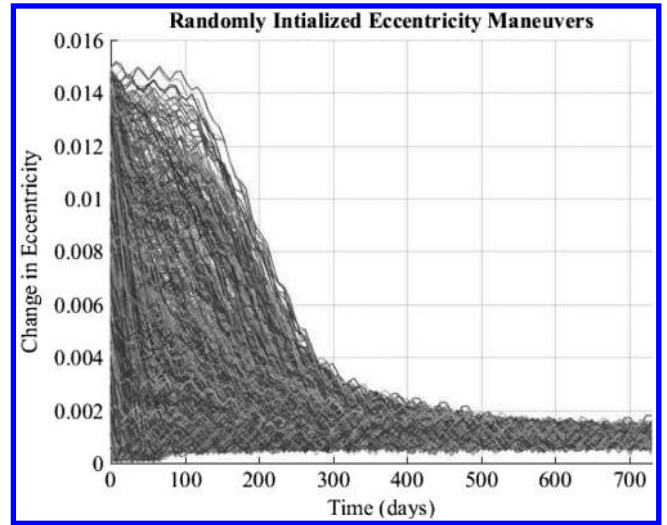

Fig. 6   Performance results of 1000 simulations to reduce eccentricity.

where α is determined using the techniques from Sec. II, and the total gravitational acceleration vector is defined as

$$\boldsymbol{a}_{\text{gravity}} = \ddot{\boldsymbol{r}}_{\oplus} + \ddot{\boldsymbol{r}}_{\mathbb{C}} + \ddot{\boldsymbol{r}}_{\odot} \qquad (44)$$

This algorithm states that the total gravitational acceleration vector must be in positive alignment with the orbital velocity vector to increase the velocity with SRP, or in negative alignment with the orbital velocity vector to decrease the velocity with SRP. If neither of the conditions of Eq. (43) are met, the sail normal must be oriented perpendicular to the sun position vector, minimizing the undesirable effects of SRP. The results of this velocity monitoring technique are illustrated in Fig. 7. The Monte Carlo analysis for the velocity monitoring technique is displayed in Fig. 8 using the same initial conditions from Table 4. Using this method, annual maximum changes in eccentricity of approximately 0.012 are possible. These sharp drops
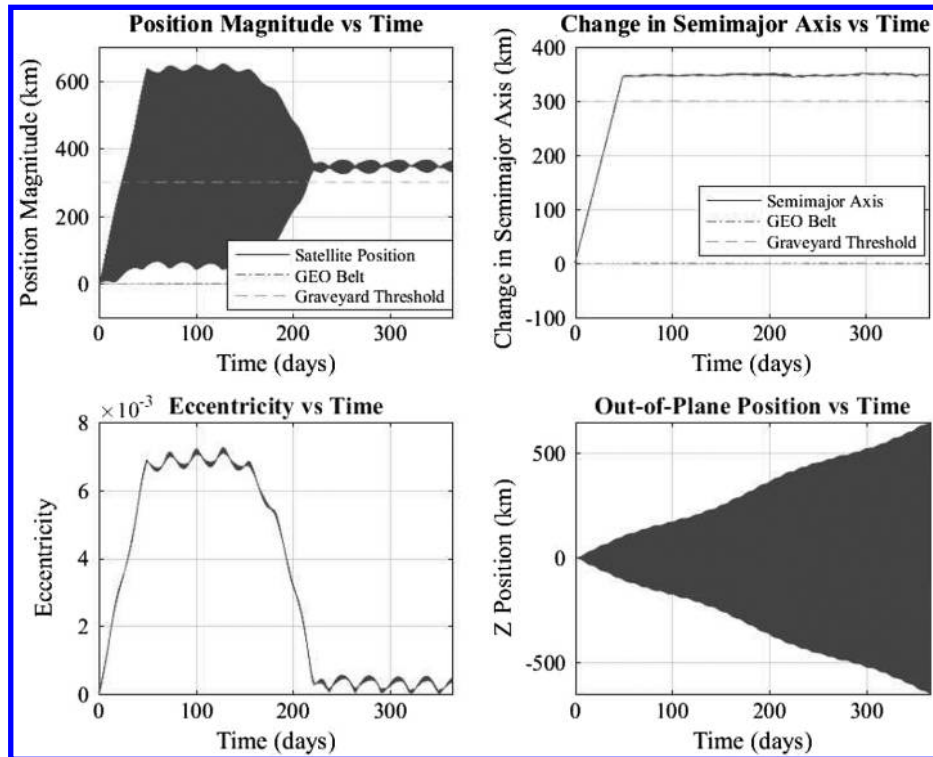
Fig. 7 Sail orientations to minimize eccentricity, using velocity monitoring technique, after raising semimajor axis. Position and semimajor axis values are zeroed at the GEO belt.
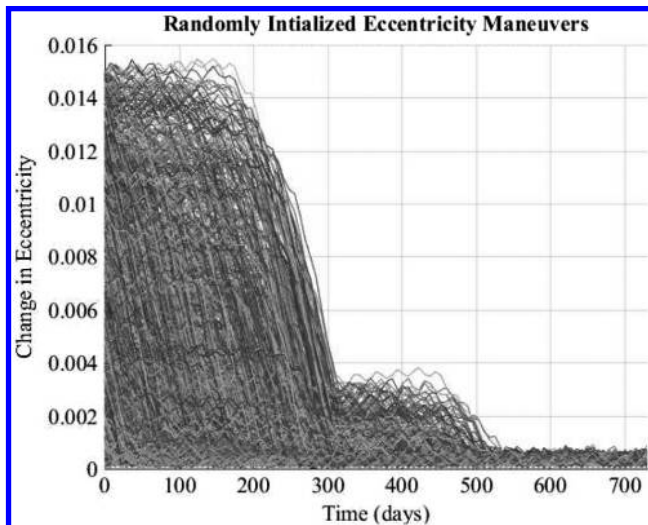

Fig. 8   Performance results of 1000 simulations to reduce eccentricity with velocity monitoring.

in eccentricity exist in periods of the orbit where beneficial vector alignments exist as outlined in Eq. (43). The performance plateaus indicate periods of poor alignment between the eccentricity and gravitational acceleration vectors. Steady-state error convergence is achieved at eccentricity values of approximately 0.001.

C.   Inclination

Throughout the orbit, TugSat is exposed to out-of-plane accelerations, which create an increase in inclination, leading to oscillations of thousands of kilometers about the equator. Although these inclinations are inconsequential during the removal of orbital debris, they can pose problems for rendezvous with a desired orbital slot. To address these drifts, an error function can be written as

$$U = \frac{1}{2}\sigma_i^2$$
$$= \frac{1}{2}(i - i_d)^2 \qquad (45)$$

with

$$\dot{U} = \sigma_i\dot{\sigma}_i$$
$$= (i - i_d)\frac{\mathrm{d}i}{\mathrm{d}t} \qquad (46)$$

to determine a control input to achieve the desired inclination i_d. As before, the expression for $\mathrm{d}i/\mathrm{d}t$ is known from Eq. (8), and sail orientations to minimize the inclination error can be found using the methods described in Sec. III.

To verify the utility of these orientations, 1000 simulations were executed with initial conditions given in Table 5. For these simulations, the satellite is without payload, characterized by an A/m ratio of 16 m^2/kg. The satellite is initialized to drift throughout the GEO belt for 180 days, accumulating inclination changes due to perturbations from Earth's oblateness and third-body accelerations. Results of these simulations can be found in Fig. 9, indicating effective reduction of planar oscillations and return of the satellite to the equatorial plane.

It is important to note that the inclination is only affected by out-of-plane accelerations (those acting along the $\hat{W}$ direction). Solutions producing the desired $\hat{W}$ acceleration may, however, include components in the $\hat{R}$ and $\hat{S}$ directions, potentially affecting the semimajor axis and eccentricity behaviors in an undesirable manner. A geometric workaround is to orient the satellite to only produce accelerations in the $\hat{W}$ direction. This approach may not achieve the desired control input from Eq. (46); however, the resulting orientation will still produce the desired effect as confirmed in simulation. Figure 10 illustrates the return to the equatorial plane using these inclination tracking orientations. Geometries during the spring and fall equinoxes account for the smaller oscillation events on the order of 30 km. Orbits occurring near the equinoxes exhibit oscillations

Table 5 Simulation properties
for inclination control tests[a]

Parameter	Range
a_0	42,164 km
e_0	0
i_0	0 rad
Ω_0	$\in [0, 2\pi]$ rad
ω_0	$\in [0, 2\pi]$ rad
ν_0	$\in [0, 2\pi]$ rad
r_z	0 km (inclination of 0 rad)

[a]Simulation durations of two years, initialized between the years 2000 and 2020.

about the equatorial plane due to the geometries of the orbit inclination and the sun direction vector. Favorable geometries simply do not exist for long enough durations during these periods to allow for continuous dampening using only $\hat{W}$ accelerations.

D. Longitude Targeting

Once TugSat has released its payload with an acceptable semimajor axis and eccentricity, return to the GEO belt commences. The return orbit requires controlled descent for placement into a desired slot within the GEO belt for rendezvous with another payload. A novel method for longitude targeting using SRP is now presented, using semimajor axis changes and their resulting effects on the satellite's angular velocity.

To begin, the orbital longitude is now defined as

$$\lambda = \omega t \tag{47}$$

where λ is the longitude of interest, ω is angular velocity of the GEO slot, and t is the time since a reference epoch. For circular orbits, the angular velocity is equivalent to the mean motion n as follows:

$$\omega = n = \sqrt{\frac{\mu}{a^3}} \tag{48}$$

The phase angle ϕ between the satellite's longitude and the desired GEO slot longitude will be defined as

$$\phi = \lambda_{\text{satellite}} - \lambda_{\text{slot}} \tag{49}$$

From Eq. (48), it is clear that the angular velocity of a satellite in circular orbit has an inverse relationship with the semimajor axis.
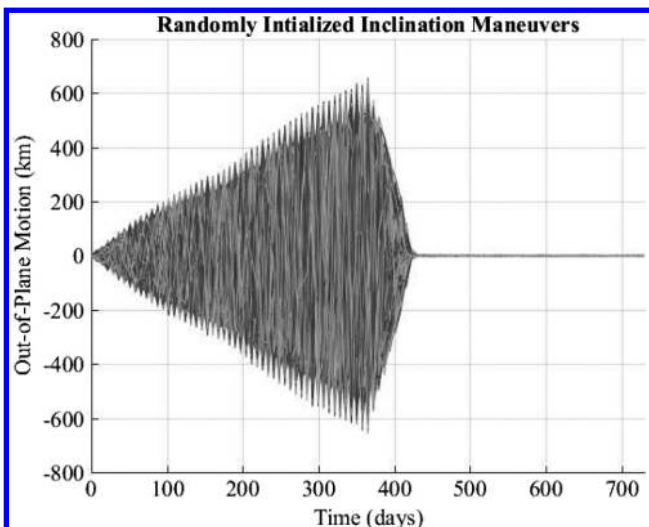
Fig. 9 Performance results of 1000 simulations to reduce eccentricity with velocity monitoring.

With this information, a satellite can speed up to a leading GEO slot by decreasing its semimajor axis or slow down to a trailing GEO slot by increasing its semimajor axis.

To derive the optimized orientations for longitude targeting, the time derivative of the longitude error ϕ must be expressed as

$$\dot{\phi} = \frac{d}{dt}(\lambda_{\text{satellite}} - \lambda_{\text{slot}}) \tag{50}$$

The angular velocity of the GEO slot is constant, so the time derivative of λ_{slot} is simply the mean motion of the slot n_{slot}. Due to the small eccentricity of the satellite orbit, the longitude derivative of the satellite will be defined as

$$\dot{\lambda}_{\text{satellite}} = n_{\text{satellite}} \tag{51}$$

resulting in

$$\dot{\phi} = n_{\text{satellite}} - n_{\text{slot}} \tag{52}$$

For longitude control, an $\dot{a}$ term is desired, which can be found by taking one more derivative:

$$\ddot{\phi} = \dot{n}_{\text{satellite}} = -\frac{3}{2}\sqrt{\frac{\mu}{a^5}}\dot{a} \tag{53}$$

From these dynamics equations, a controller can be designed to reduce the longitude error using the time derivative of the satellite's mean motion.

The candidate error function will be defined as

$$U = \frac{1}{2}\phi^2 + \frac{1}{2}\eta^2 \tag{54}$$

with error derivative

$$\dot{U} = \phi\dot{\phi} + \eta\dot{\eta} \tag{55}$$

The η term is a backstepping error defined as the difference between the satellite's mean motion and the satellite's desired mean motion n_d:

$$\eta = n_{\text{satellite}} - n_d \tag{56}$$

$$\dot{\eta} = \dot{n}_{\text{satellite}} - \dot{n}_d \tag{57}$$

This error will be used to drive ϕ to zero using an unmatched control input. To introduce the backstepping error into the dynamics, Eq. (52) is rewritten as

$$\dot{\phi} = n_{\text{satellite}} - n_{\text{slot}} + n_d - n_d$$
$$= \eta - n_{\text{slot}} + n_d \tag{58}$$
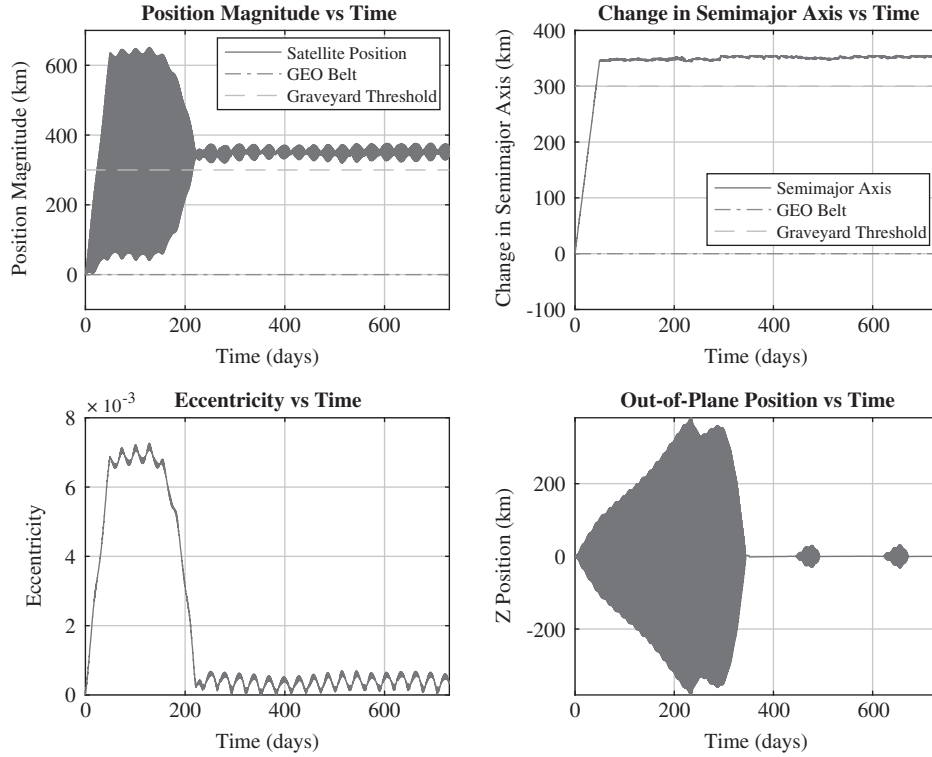
Next, Eq. (53) will be used with Eq. (57), resulting in

$$\dot{\eta} = -\frac{3}{2}\sqrt{\frac{\mu}{a^5}}\dot{a} - \dot{n}_d \tag{59}$$

Inserting these expressions into Eq. (55), the error derivative can now be rewritten as

$$\dot{U} = \phi(\eta - n_{\text{slot}} + n_d) + \eta\left(-\frac{3}{2}\sqrt{\frac{\mu}{a^5}}\dot{a} - \dot{n}_d\right) \tag{60}$$

Equation (60) can be made nonpositive through the appropriate design of n_d and $\dot{a}$. A suitable design is presented as follows:

$$n_d = n_{\text{slot}} - k\phi \tag{61}$$

Fig. 10 Sail orientations to minimize inclination deorbit and release of payload. Position and semimajor axis values are zeroed at the GEO belt.

$$\dot{a} = -\frac{2}{3}\sqrt{\frac{a^5}{\mu}}(\dot{n}_d - k\phi - k\eta) \qquad (62)$$

Combining Eqs. (60–62) results in

$$\begin{aligned}
\dot{U} &= \phi(k\eta - n_{\text{slot}} + n_{\text{slot}} - k\phi) \\
&\quad + \eta\left(-\frac{3}{2}\sqrt{\frac{\mu}{a^5}}\left\{-\frac{2}{3}\sqrt{\frac{a^5}{\mu}}(\dot{n}_d - k\phi - k\eta)\right\} - \dot{n}_d\right) \\
&= -k\phi^2 + k\phi\eta + \eta(\dot{n}_d - k\phi - k\eta - \dot{n}_d) \\
&= -k\phi^2 + k\phi\eta - k\eta\phi - k\eta^2 \qquad (63)
\end{aligned}$$

ultimately yielding the nonpositive error derivative:

$$\dot{U} = -k\phi^2 - k\eta^2 \qquad (64)$$

Sail orientation angles can be determined by equating Eqs. (23) and (62):

$$\begin{aligned}
-\frac{2}{3}\sqrt{\frac{a^5}{\mu}}(\dot{n}_d - k\phi - k\eta) &= \boldsymbol{\zeta}_a \cdot \boldsymbol{\Gamma}_{\text{SRP}} \\
&= -a_c\|\boldsymbol{\zeta}_a\|\cos^3\delta[\cos^2\alpha(\cos\alpha\cos\beta \\
&\quad + \sin\alpha\sin\beta)] \qquad (65)
\end{aligned}$$

Choosing $\delta = 0$ and recalling the definition of ρ_a as the product of a_c and $\|\boldsymbol{\zeta}_a\|$, Eq. (65) becomes

$$\frac{2(\dot{n}_d - k\phi - k\eta)}{3\rho_a}\sqrt{\frac{a^5}{\mu}} = \cos^2(\alpha)\cos(\alpha - \beta) \qquad (66)$$

Note that, for longitude targeting, n_d is a constant ($\dot{n}_d = 0$) equal to n_{slot}. The constants on the left-hand side of Eq. (66) can be combined to form ρ_ϕ:

$$\rho_\phi = -\frac{2k(\phi + \eta)}{3\rho_a}\sqrt{\frac{a^5}{\mu}} \qquad (67)$$

A cost function J_ϕ can be expressed as

$$J_\phi = |\rho_\phi - \cos^2(\alpha)\cos(\alpha - \beta)| \qquad (68)$$

As before, the desired orientations can be found by minimizing J_ϕ across the interval

$$\alpha \in \left[-\frac{\pi}{2}, \frac{\pi}{2}\right]$$

With α determined, an algorithm to implement the longitude tracking orientations is presented as

if

$$\phi > 0 \quad \text{and} \quad a < a_d$$

or

$$\phi < 0 \quad \text{and} \quad a > a_d$$

then

$$\hat{\boldsymbol{n}} = \cos\alpha\hat{\boldsymbol{e}}_1 + \sin\alpha\hat{\boldsymbol{e}}_2 \qquad (69)$$

This algorithm addresses positive phase angles by raising the semimajor axis and negative phase angles by lowering the semimajor axis using the optimized orientations. Figure 11 illustrates longitude targeting using this algorithm.

To gauge the performance of the longitude targeting method, 1000 simulations were run to analyze error convergence and targeting times. Initial semimajor axis values ranged within GEO $\pm$ 500 km and launch dates fell between the years 2000 and 2020. Longitude values were randomized across all angles $\in [0, 2\pi]$. Steady-state error convergence was obtained within 2 deg in 10 years for 92.8% of the simulations. The results of these simulations are contained in Fig. 12. To explain the convergence behaviors, targeting scenarios are divided
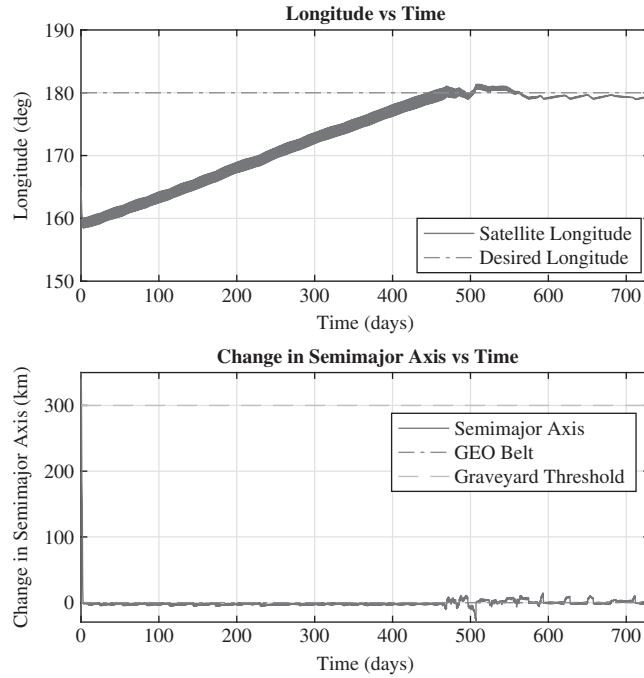
Fig. 11   Sail orientations to target desired GEO belt longitude using control of semimajor axis. Semimajor axis values are zeroed at the GEO belt.
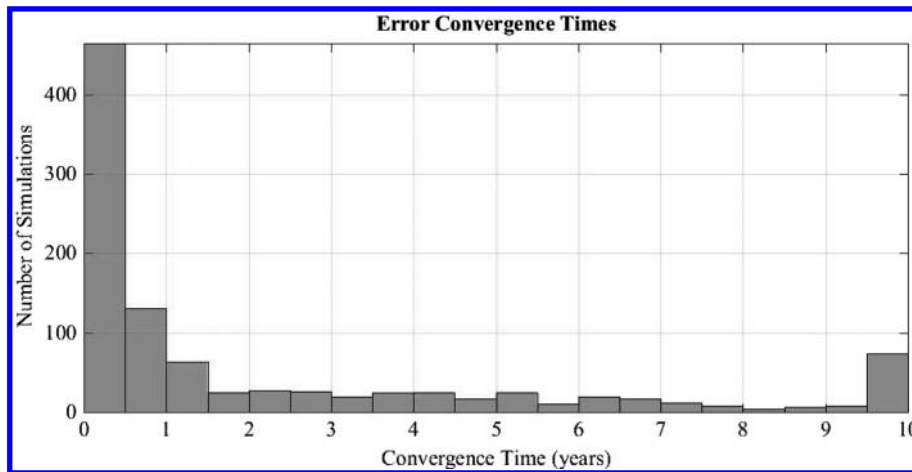

Fig. 12   Convergence times for 1000 longitude targeting simulations. Simulations requiring 10 years or longer for convergence are collected in the final bin.

into two cases as described in Table 6. It is observed that targeting maneuvers initialized with longitude and semimajor axis errors corresponding to case A are capable of error convergence within two years. Initial conditions falling under case B can take significantly longer to achieve error convergence. Figure 13 displays targeting times based on initial phase angles for each case. From these results, it is apparent that successful longitude targeting times depend upon the initial relationship between the phase angle and semimajor axis error.

E.   Deorbit Simulation

With the primary maneuvers outlined, the entire TugSat simulation can be presented. The simulation will begin with TugSat and the payload in a perfectly circular, equatorial orbit. Specifically, TugSat

will deorbit the payload by increasing the apogee and raising the semimajor axis 350 km above the GEO altitude. Once the desired semimajor axis is achieved, TugSat will reduce the eccentricity of the orbit before releasing the payload to drift in a disposal orbit as outlined in Table 2. After releasing the payload, Tugsat will return to the GEO belt, targeting its initial longitude from the start of the simulation. This longitude has been chosen arbitrarily in order to demonstrate successful targeting of a desired GEO slot. During rendezvous with the GEO slot, TugSat will reduce its inclination, returning to an equatorial orbit with increased performance due to the increase in the A/m ratio without payload. TugSat will successfully complete its mission upon rendezvous with the targeted GEO slot within the bounds defined in Table 1. Figure 14 displays the TugSat simulation.

TugSat successfully deorbits and releases its payload in less than a year. In under a year and a half, TugSat successfully returns to the GEO slot as defined by the IADC. The simulation continues to allow TugSat to further reduce eccentricity and inclination errors. In under two years from the start of the deorbit maneuver, TugSat reduces the out-of-plane motion to within 5 km while maintaining steady-state semimajor axis, eccentricity, and phase error values. This terminal
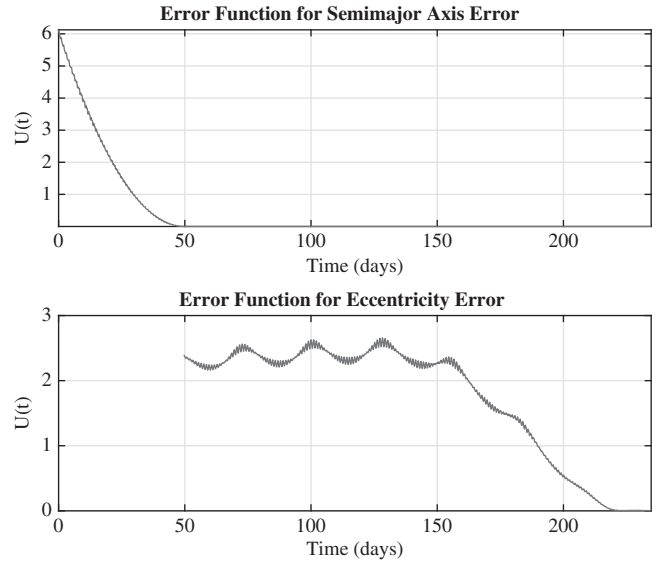
Table 6   Longitude targeting cases

Case	
A	sgn$\phi \cdot$ sgn$(a - a_d) > 0$
B	sgn$\phi \cdot$ sgn$(a - a_d) < 0$
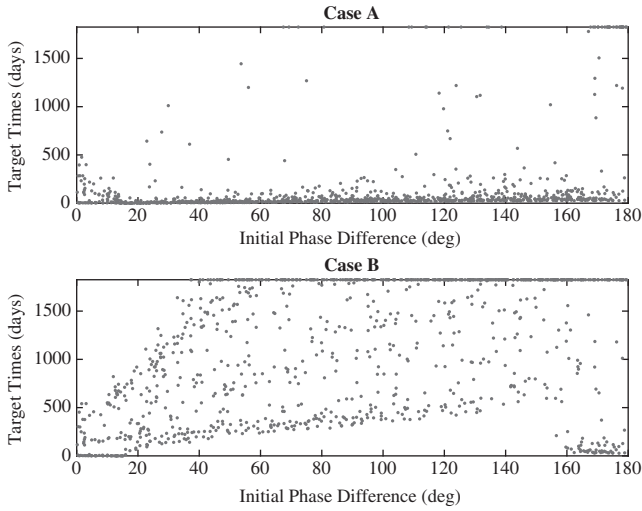
Fig. 13   Target times for favorable phase angle and semimajor axis relationships (case A) and unfavorable phase angle and semimajor axis relationships (case B).

Fig. 15   Error functions during deorbit phase of TugSat simulation.
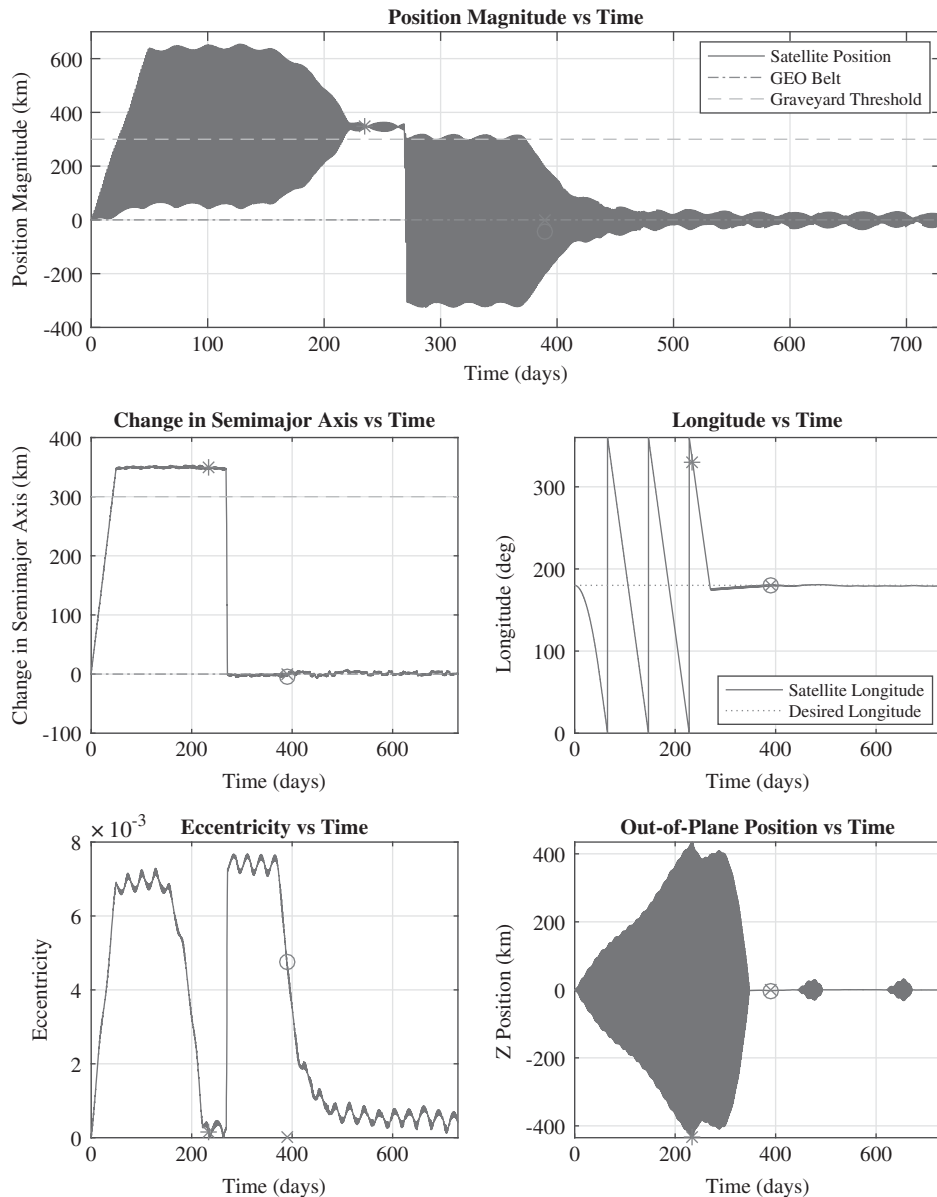
Fig. 14   TugSat simulation results. Star denotes release of payload, circle denotes successful targeting of GEO belt longitude based on IADC guidelines, and cross denotes ideal value for rendezvous.
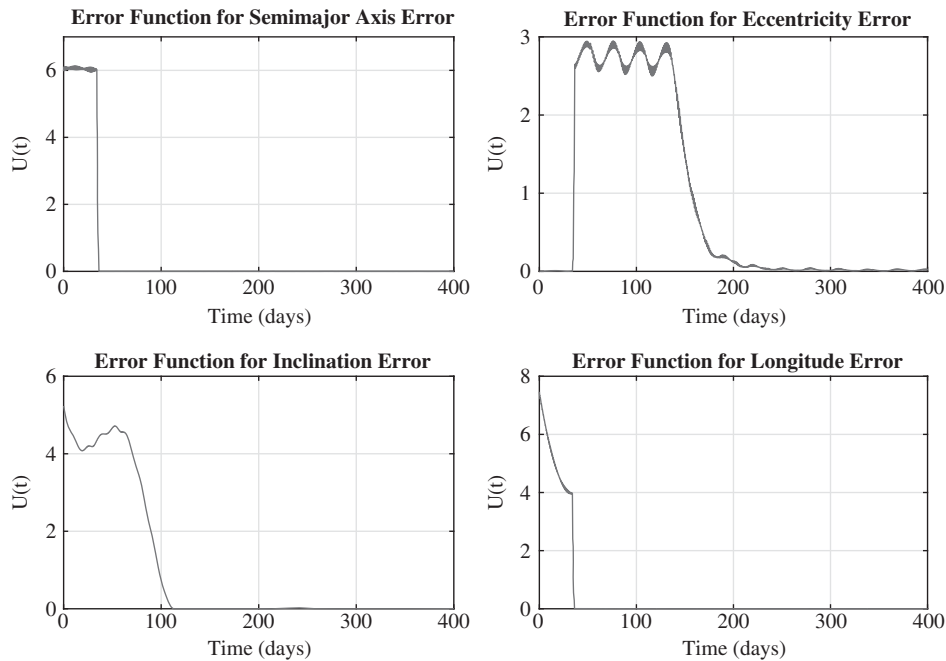
Fig. 16 Error functions during reorbit phase of TugSat simulation.

placement is well suited for the spacecraft to begin proximity operations using relative motion equations for rendezvous with the new payload.

Figures 15 and 16 plot the error functions for the TugSat simulation to gauge the performance of the optimized sail orientations. These figures analyze the performance during the deorbit and reorbit phases of the simulation. Recall that satellite deorbit does not have inclination or longitude requirements. The error functions decrease nonmonotonically due to the switching between control of semimajor axis, eccentricity, inclination, and longitude and the presence of the gravitational perturbations. From Figs. 15 and 16, the optimized sail orientations prove effective, even under the influence of the full dynamics model.

For this simulation, deorbit and reorbit maneuvers were completed with a delta-V of 0.3 and 0.17 km/s, respectively, without the use of conventional thrusters for propulsion. Although the satellite was able to return to the desired GEO location, actual rendezvous with a second payload would require assistance from thrusters for fine maneuvering and successful docking with the payload. By repeating these maneuvers, multiple GEO slots can be made available for reuse using a single solar sailing satellite.

V. Conclusions

Solar radiation pressure serves as a powerful resource for satellites in high-altitude orbits, particularly geosynchronous equatorial orbit (GEO), providing an avenue for low-precision indefinite satellite maneuvering with virtually infinite delta-V. Solar sailing can help to reduce propellant dependencies, allowing for the allocation of resources on larger payloads, more sensors, or the elongation of a satellite's operational lifespan. With the continued trend toward miniaturization, solar radiation pressure (SRP) may become a viable means of propulsion for many future satellites.

Inspired by the present capabilities of solar sailing technology, the TugSat simulation outlines one potential solar sailing application. Using a spacecraft on the scale of a 6U CubeSat ($30 \times 20 \times 10 \times$ cm), sufficient delta-V can be provided to deorbit space debris many times more massive than the solar sailing satellite itself. Control techniques determined using optimized vector geometries, along with the Gaussian variation of parameters equations, have been proven to produce sail orientations that obtain desired orbital element values. Through intelligent switching between control of the orbital elements, the TugSat simulation allows for orbital debris removal and subsequent GEO slot rendezvous in under two years without reliance on traditional propulsion

systems. Although stability could not be proven analytically, the Monte Carlo results validated the effectiveness of these orientations. Supplementing these maneuvers with thrusters for time-sensitive fine maneuvering would greatly enhance the capabilities of a solar sailing mission and open the door for precision rendezvous and docking using solar sailing satellites.

This work provides methods that may prove useful for orbit on other celestial bodies where SRP is capable of combating accelerations in a local environment. As a follow up to this research, the challenge of satellite rendezvous with orbital debris using sail-assisted propulsion can be investigated. Additionally, these findings can be used to investigate time-optimal trajectories that effectively leverage gravitational perturbations with SRP to achieve desired orbits. Using SRP, any number of solar sailing missions can be performed using tactful combinations of these presented maneuvers.

References

[1] "IADC Space Debris Mitigation Guidelines," Inter-Agency Space Debris Coordination Committee Rept. IADC-02-01, Rev. 1, Sept. 2007.
[2] "Support to the IADC Space Debris Mitigation Guidelines," Inter-Agency Space Debris Coordination Committee Rept. IADC-02-01, Rev. 5.5, May 2014.
[3] Jehn, R., Agapov, V., and Hernández, C., "The Situation in the Geostationary Ring," *Advances in Space Research*, Vol. 35, No. 7, 2005, pp. 1318–1327.
    doi:10.1016/j.asr.2005.03.022
[4] Castet, J.-F., and Saleh, J. H., "Satellite and Satellite Subsystems Reliability: Statistical Data Analysis and Modeling," *Reliability Engineering and System Safety*, Vol. 94, No. 11, 2009, pp. 1718–1728.
    doi:10.1016/j.ress.2009.05.004
[5] Allen, J., "The Galaxy 15 Anomaly: Another Satellite in the Wrong Place at a Critical Time," *Space Weather*, Vol. 8, No. 6, 2010, Paper S06008.
    doi:10.1029/2010SW000588
[6] Missel, J., and Mortari, D., "Removing Space Debris Through Sequential Captures and Ejections," Vol. 36, No. 3, 2013, pp. 743–752.
    doi:10.2514/1.58768

[7] Schaub, H., and Moorer, D. F., "Geosynchronous Large Debris Reorbiter: Challenges and Prospects," *Journal of the Astronautical Sciences*, Vol. 59, No. 1, 2012, pp. 161–176.
doi:10.1007/s40295-013-0011-8

[8] Estes, R. D., Lorenzini, E. C., Sanmartin, J., Pelaez, J., Mart-egrave, M., Johnson, C. L., and Vas, I. E., "Bare Tethers for Electrodynamic Spacecraft Propulsion," *Journal of Spacecraft and Rockets*, Vol. 37, No. 2, 2000, pp. 205–211.
doi:10.2514/2.3567

[9] Bevilacqua, R., and Romano, M., "Rendezvous Maneuvers of Multiple Spacecraft Using Differential Drag Under J2 Perturbation," *Journal of Guidance, Control, and Dynamics*, Vol. 31, No. 6, 2008, pp. 1595–1607.
doi:10.2514/1.36362

[10] McInnes, C. R., "Solar Sailing: Mission Applications and Engineering Challenges," *Philosophical Transactions of the Royal Society of London, Series A: Mathematical, Physical and Engineering Sciences*, Vol. 361, No. 1813, 2003, pp. 2989–3008.
doi:10.1098/rsta.2003.1280

[11] McInnes, C. R., "Solar Sailing: Orbital Mechanics and Mission Applications," *Advances in Space Research*, Vol. 31, No. 8, 2003, pp. 1971–1980.
doi:10.1016/S0273-1177(03)00172-8

[12] Hur, S., and Bryson, A., Jr., "Minimum Time Solar Sailing from Geosynchronous Orbit to the Sun-Earth L2 Point," *Astrodynamics Conference, AIAA Guidance, Navigation, and Control and Co-Located Conferences*, AIAA Paper 1992-4657, 1992.
doi:10.2514/6.1992-4657

[13] Quarta, A. A., and Mengali, G., "Approximate Solutions to Circle-to-Circle Solar Sail Orbit Transfer," *Journal of Guidance, Control, and Dynamics*, Vol. 36, No. 6, 2013, pp. 1886–1890.
doi:10.2514/1.60307

[14] Wie, B., "Thrust Vector Control of Solar Sail Spacecraft," "AIAA Guidance, Navigation, and Control Conference and Exhibit," *AIAA Guidance, Navigation, and Control and Co-Located Conferences*, AIAA Paper 2005-6086, 2005.
doi:10.2514/6.2005-6086

[15] Lücking, C., Colombo, C., and McInnes, C. R., "Solar Radiation Pressure-Augmented Deorbiting: Passive End-of-Life Disposal from High-Altitude Orbits," *Journal of Spacecraft and Rockets*, Vol. 50, No. 6, 2013, pp. 1256–1267.
doi:10.2514/1.A32478

[16] Lücking, C., Colombo, C., and McInnes, C. R., "A Passive Satellite Deorbiting Strategy for Medium Earth Orbit Using Solar Radiation Pressure and the J2 Effect," *Acta Astronautica*, Vol. 77, Aug.–Sept. 2012,

pp. 197–206.
doi:10.1016/j.actaastro.2012.03.026

[17] Coverstone, V. L., and Prussing, J. E., "Technique for Escape from Geosynchronous Transfer Orbit Using a Solar Sail," *Journal of Guidance, Control, and Dynamics*, Vol. 26, No. 4, July 2003, pp. 628–634.
doi:10.2514/2.5091

[18] Borja, J. A., and Tun, D., "Deorbit Process Using Solar Radiation Force," *Journal of Spacecraft and Rockets*, Vol. 43, No. 3, 2006, pp. 685–687.
doi:10.2514/1.9508

[19] Tsuda, Y., Mori, O., Funase, R., Sawada, H., Yamamoto, T., Saiki, T., Endo, T., Yonekura, K., Hoshino, H., and Kawaguchi, J., "Achievement of IKAROS-Japanese Deep Space Solar Sail Demonstration Mission," *Acta Astronautica*, Vol. 82, No. 2, 2013, pp. 183–188.
doi:10.1016/j.actaastro.2012.03.032

[20] Biddy, C., and Svitek, T., "LightSail-1 Solar Sail Design and Qualification," *Proceedings of the 41st Aerospace Mechanisms Symposium*, NASA CP-2012-217653, May 2012, pp. 451–463.

[21] Heiligers, J., Diedrich, B., Derbes, W., and McInnes, C., "Sunjammer: Preliminary End-to-End Mission Design," *AIAA/AAS Astrodynamics Specialist Conference, AIAA SPACE Forum*, AIAA Paper 2014-4127, 2014.

[22] McNutt, L., Johnson, L., Kahn, P., Castillo-Rogez, J., and Frick, A., "Near-Earth Asteroid (NEA) Scout," *AIAA SPACE 2014 Conference and Exposition, AIAA SPACE Forum*, AIAA Paper 2014-4435, 2014.
doi:10.2514/6.2014-4435

[23] Montenbruck, O., and Gill, E., *Satellite Orbits: Models, Methods and Applications*, 1st ed., Springer–Verlag, Berlin, 2000, pp. 53–116, Chap. 3.
doi:10.1007/978-3-642-58351-3

[24] Liu, H. S., and Chao, B. F., "The Earth's Equatorial Principal Axes and Moments of Inertia," *Geophysical Journal International*, Vol. 106, No. 3, 1991, pp. 699–702.
doi:10.1111/gji.1991.106.issue-3

[25] Lara, M., and Elipe, A., "Periodic Orbits Around Geostationary Positions," *Celestial Mechanics and Dynamical Astronomy*, Vol. 82, No. 3, 2002, pp. 285–299.
doi:10.1023/A:1015046613477

[26] Vallado, D. A., *Fundamentals of Astrodynamics and Applications*, 4th ed., Space Technology Library, Microcosm Press, Hawthorne, CA, 2013, pp. 609–730, Chap. 9.

D. A. Spencer
Associate Editor